Processability and Microstructural Evolution of W360 Hot Work Tool Steel by Directed Energy Deposition

Metals and Materials International (2024) 30:501–516
https://doi.org/10.1007/s12540-023-01508-5

Processability and Microstructural Evolution of W360 Hot Work Tool Steel by Directed Energy Deposition

Josip Vinčić[1,2] · Alberta Aversa[1] · Mariangela Lombardi[1] · Diego Manfredi[1,2]

Received: 20 April 2023 / Accepted: 20 July 2023 / Published online: 4 September 2023

Abstract
Laser directed energy deposition (L-DED) was used to produce samples of the newly patented W360 hot work tool steel by Böhler. The process parameters were optimized to obtain nearly fully dense samples through the production and analysis of single deposited tracks and single layers. Subsequently, bulk samples underwent a hardening heat treatment, consisting of austenitizing, air quenching, and tempering. The samples were analysed in the as-built condition (AB), after quenching (Q) and following tempering cycles (HT) to observe the microstructural evolution. The microstructure was investigated using optical and scanning electron microscopes, energy dispersive X-ray analysis, and X-ray diffraction analysis. Furthermore, the microstructural evolution was analysed with differential scanning calorimetry, while the mechanical response was evaluated through microhardness test. It was found that the AB samples exhibited a dendritic-cellular microstructure with tempered martensite laths. The thermal history of the AB samples was completely modified by the austenitizing treatment followed by quenching, resulting in a fully martensitic Q sample that did not display the typical dendritic-cellular microstructure of the L-DED process. The completion of the heat treatment with tempering cycles revealed the presence of Mo-rich carbides dispersed in a martensitic matrix. The HT samples exhibited a mean microhardness of 634 HV, remaining constant along the entire building direction from the substrate to the last deposited layer, indicating a homogeneous microstructure. This high value, similar to other hot work tool steels such as H13, makes W360 a very promising candidate for tool build and repair purposes.

Keywords Additive manufacturing · Laser directed energy deposition (L-DED) · Hot work tool steel W360 · Optimization of process parameters · Heat treatment · Microhardness

1 Introduction

In the 1990s, the first Additive Manufacturing (AM) technologies dedicated to metallic materials were invented and patented [1]. Over time, these technologies have improved, evolving from the creation of scale models to rapid prototyping and then to the production of structural and functional near-net-shape components. Recently, numerous companies in various industrial fields have adopted AM as an integral part of their business processes [2]. The most common AM techniques for processing metals today are Powder Bed Fusion (PBF) and Directed Energy Deposition (DED) [3]. In PBF, a thin layer of powder material is spread on a flat surface of a building platform within a closed chamber in an inert atmosphere. A focused heat source, that can be a laser (L-PBF) or an electron beam (E-PBF), is used to selectively melt the desired areas of the powder bed with an extremely fast gradient. Subsequently, the material solidifies rapidly, enabling the production of complex geometric parts with very fine microstructures [4]. On the other hand, DED systems involve the melting of material in either powder or wire form using focused thermal energy during the deposition process. As the deposition head with the heat source moves away, the molten metallic material cools and solidifies rapidly, leaving a thin track of solidified metal welded on the underlying layer. By repeating this process with multiple overlapping tracks, a complete layer is

✉ Josip Vinčić
josip.vincic@polito.it

[1] Department of Applied Science and Technology (DISAT), Politecnico di Torino, Corso Duca Degli Abruzzi, 24, 10129 Turin, Italy

[2] Istituto Italiano di Tecnologia (IIT), Center for Sustainable Future Technologies CSFT@Polito, Via Livorno 60, 10144 Turin, Italy

formed. Powder-based DED systems commonly utilize laser as a thermal energy source, while wire-based DED systems employ electric or plasma arcs, lasers, or electron beams [5–7]. In a typical DED machine, the deposition head and working table are controlled by multi-axis CNC systems, enabling precise material deposition at specific locations [8]. It is important to note that DED does not necessitate a powder bed, does not have the limitations of a closed building chamber, and can be used not only for building full parts, but also for repair or adding new material to existing objects [9]. However, due to the higher energy source and consequently slower melting and solidification compared to PBF systems, parts produced using DED typically exhibit a coarser grain size.

Different DED processes are available on the market, depending on the type of feedstock and power source employed. The most common process for processing materials in powder form is Laser-DED (L-DED), which is also known as Laser Metal Deposition (LMD), Laser Cladding (LC), or Laser Engineered Net Shaping (LENS) [10]. In line with the global goal of sustainability, repairing and remanufacturing damaged parts are considered more desirable solutions than producing new parts, especially in terms of energy consumption [11]. In comparison to traditional welding technologies used for repair, such as Tungsten Inert Gas (TIG) welding, Plasma Transferred Arc Welding (PTAW), and Electron Beam Welding (EBW), L-DED shows great potential due to lower residual stresses, higher repeatability, and increased precision [12, 13]. However, it is known that parts produced by L-DED often exhibit non-uniform microstructures and properties, which limits their application [8, 14]. This non-uniformity arises from the complex thermal history experienced by the manufactured samples. A cross section of a DED sample along the building direction can be schematically subdivided into four zones. Starting from the substrate material the first zone is the "not affected zone". Then, closed to the first layer deposited, there is the "heat-affected zone". Then the third zone consists of "tempered metal", which corresponds to the main deposited part, while the top layer of the sample, corresponding to the last deposited layer, form the "non-tempered metal" zone [15, 16] During the process, the first layer is usually deposited on a cold substrate at environment temperature, causing rapid cooling due to the dissipation of heat and leaving a non-tempered layer. With each additional layer deposition, the heat from the energy source to the solidifying material passes through the previously deposited layers into the substrate, causing an intrinsic heat treatment (IHT) effect. However, the last layer deposited does not undergo this reheating process, and therefore it exhibits a microstructure characteristic of the as-built material [17–19]. Therefore, to achieve uniform microstructure and hence uniform mechanical properties in bulk samples by L-DED, post-processing heat treatments are commonly utilized [20, 21]

When considering materials, a number of them have been explored by L-DED. Generally, metallic materials that exhibit reasonably good weldability are easier to process, while metals with high reflectivity and thermal conductivity are difficult to process, such as gold and certain alloys of aluminum and copper [22, 23]. Moreover, if the focus is on using L-DED for repairing tools, the main material requirements are very high mechanical properties, such as high yield strength, high hardness and abrasion resistance. In such cases, steels, particularly tool steels would be the preferred choice [24]. Tool steels belong to a family of high-carbon and alloyed steels with specific characteristics including very high hardness (exceeding 600 HV), excellent wear resistance, and toughness even at elevated temperatures. They find wide application in various tools and tooling systems, including dies, moulds, and cutting tools. Tool steels are typically categorized into six groups: water-hardening, cold-work, shock-resistant, high-speed, hot work, and special purpose steels [25]. Due to their high market value, the repair of worn or damaged tool steel components holds significant importance across numerous industries [26].

Among tool steels, only a few grades have been successfully processed by L-DED [27]. Tool steels are generally high-alloyed carbon steels, and most of them have an equivalent carbon content of over 0.50% according to the European standard EN 1011–2 Method A, Eq. (1) [28].

$$CE = \%C + \frac{\%Mn}{6} + \frac{\%Cr + \%Mo + \%V}{5} + \frac{\%Cu + \%Ni}{15} \quad (1)$$

In welding literature, it is reported that steels with an equivalent carbon content exceeding 0.7% are considered non-weldable or, at least, difficult to weld. This is due to their tendency to form martensite upon cooling, leading to increased sensitivity to cold cracking. Cold cracking is associated with changes in the specific volume during the solid-phase transformation [29–32].

Considering hot work tool steels, the most investigated in the AM field are chromium-molybdenum steels, with the AISI H13 (1.2344, X40CrMoV5-1) grade being particularly prominent [27]. Despite H13 steel having a relatively high processability indicator equivalent carbon content of 2.14% according to Eq. (1), its remarkable combination of hardness, toughness, thermal shock resistance, and wear resistance make it highly desirable [33]. Extensive studies have been conducted on H13 steel produced by both PBF and L-DED, as reported in literature [14, 15, 17–19, 27, 34–36]. It has been demonstrated that dense and crack free samples of H13 can be achieved through L-DED by optimizing the main process parameters. However, there are still challenges

that need to be addressed, including locally varying heat transfer rates during manufacturing, which directly affect cooling rates and subsequent changes in microstructure. As stated before, the layer by layer deposition process in L-DED results in IHT, involving repeated heating, austenitizing and tempering. The formation of martensite, re-austenitization, and tempering effects strongly depend on the process parameters and position within the parts along the building direction. At the tip of the part, corresponding to the last layer deposited, no further reheating occurs, and martensite forms without subsequent re-austenitization or tempering. As result, the hardness within the as-built samples can vary along the building direction due to IHT, necessitating post-heat treatment for homogenization. Typically, this involves austenitization followed by quenching and one or more tempering cycles [14, 21, 37].

Bohlen et al. and Mazumder et. al reported that the microstructure of H13 produced by L-DED in as-built condition consists of solidification cells and dendrites with retained austenite located in the interdendritic regions. The size of these cells ranges from 2 to 30 µm [38]. The cellular structure is the result of micro-segregation during solidification, which leads to enrichment of certain alloying elements, such as Cr, Mo and V in the interdendritic regions. Carbide precipitates can already be present in the as built condition. The lower layers, which undergo IHT, contain carbides rich in V and Cr. These carbides are mainly MC-type carbides, along with a small amount of M_7C_3 carbides. For as-built material produced by L-DED, the hardness ranges from 550 to 660 HV [27, 38, 39], the ultimate tensile strength (UTS) is around 2000 MPa and the elongation at fracture ranges from 5 to 6%, which is similar to the values of quenched and tempered wrought material, reflecting its in-situ tempered state [27].

Other tool steels that have been processed by L-DED include high-speed tool steels M2, M4, and CPM 9 V, as well as the recently introduced cold-work tool steel D2 [40–43]. Die repairing applications using CPM 9 V on H13 tool steel and mould repair using H13 have shown that repairing tool steel parts using L-DED results in similar mechanical properties to those of the original parts [32, 44, 45].

Very recently a new hot work tool steel named W360, patented by voelstalpine Böhler, has been available on the market of AM powders. It has been designed to outperform other tool steels like M300 or H13, exhibiting higher toughness and wear resistance at high temperatures. According to the Bohler datasheet, after a tempering heat treatment in order to achieve a hardness of 590–630 HV, additively manufactured W360 parts can exhibit a range of properties, including a UTS of ranging from 1970 to 2010 MPa, yield strength between 1500 and 1670 MPa, elongation ranging from 6.6 to 8.1%, and the reported toughness between 8 and 14 J/cm^2 [46]. These exceptional properties make it an excellent candidate for demanding tooling applications like High Pressure Die Casting (HPDC). The equivalent carbon content of W360 steel, calculated using Eq. (1), is 2.15%, indicating similar processability by AM to H13. However, to the best of the authors' knowledge, there are no previous studies in the literature on the processing of W360 through L-DED or through other AM techniques [47].

Considering this, the main focus of this study to evaluate the processability of the new hot work tool steel, W360, by L-DED, trying to expand the existing database of tool steel grades available for this technology. The experimental investigation begins with the optimizing of L-DED process parameters specifically for W360 steel, with the ultimate goal of achieving fully dense bulk samples without cracks. This optimization process involves fabricating single tracks (STs), followed by single layers (SLs), and finally parallelepiped bulk samples. The optimal energy density is determined by depositing STs using different combinations of power and scan speed. Additionally, SLs are manufactured to determine the layer thickness for subsequent bulk sample deposition. Once the feasibility of producing dense and crack-free bulk samples is demonstrated, a hardening heat treatment, commonly used for other hot work tool steels, is applied to achieve a uniform microstructure with consistent mechanical properties. This heat treatment consists of austenitization, followed by quenching and three subsequent tempering cycles. Characterization of the W360 steel L-DED samples in various post-processing conditions provides an initial understanding of their microstructure. The microstructural evolution is examined throughout the entire heat treatment process, starting with the analysis of the as-built (AB) condition, followed by investigations after air quenching (Q), and culminating with evaluations after the three consecutive tempering cycles (HT). The samples labelled AB, Q, and HT are examined using Optical and Field Emission Scanning Electron Microscopy (OM and FESEM), in conjunction with Energy Dispersive X-Ray (EDX) and X-Ray Diffraction (XRD) analyses, to gather information about their chemical composition and about the phase evolution. Differential Scanning Calorimetry (DSC) is employed to study the phase transformations during tempering while microhardness tests provide an initial assessment of the samples mechanical response. This research effort demonstrates, for the first time, the processability of W360 tool steel by L-DED and could establish a rapid and reliable procedure for optimizing process parameters. The exploration of W360 steel at different stages of heat treatment opens new possibilities for utilizing this remarkable hot work tool steel grade in AM applications, ranging from the production of complex components, like moulds with internal cooling channels, to the use in mould and tool repair.

Table 1 Nominal chemical composition of the W360 steel powder used in this study

Composition	C	Si	Mn	Cr	Mo	V	Fe
Wt. %	0.50	0.20	0.25	4.5	3.0	0.55	Bal

2 Materials and Methods

2.1 Materials

A commercially available gas atomized W360 tool steel powder from voelstalpine Böhler Edelstahl GmbH & Co, a special steel producer located in Styria (Austria), with a chemical composition presented in Table 1, was utilized for the production of AM samples using L-DED. The producer stated also that the powders are atomized using renewable electrical energy and that they are one hundred percent recyclable. The powder was characterized as-received through laser granulometry and SEM. As depicted in Fig. 1, the W360 powder exhibited a unimodal Gaussian particle size distribution, with d10, d50, and d90 values of 45.2, 76.0, and 131.3 µm, respectively. Hence, it could be stated that it falls within the typical range for L-DED processes, which is 50–150 µm. SEM images presented in Fig. 2 display predominantly spherical-shaped particles, along with numerous small satellites (Fig. 2b). Additionally, the images reveal the presence of some agglomerated small particles (Fig. 2c). Such morphology is common for gas atomized powders, as smaller droplets, possessing higher velocities, may collide with larger droplets, resulting in adhesion on the surface and the formation of satellite powder [48]. Nevertheless, this phenomenon should not significantly impact the processability of the material during L-DED, as it is unrelated to powder bed behaviour.

2.2 Experimental Procedure

The L-DED system used is a Laserdyne 430 by Prima Additive (Fig. 3). A 3-axis CNC unit was used to control X–Y movements of the deposition table and the Z movement of deposition head. The machine is equipped with a fibre laser with maximum power output of 1 kW and nominal laser spot diameter (d_l) of 2 mm. A commercial powder feeder was used to transfer powder to the deposition head, with four coaxial multi-nozzles (4-way). Argon with 99.99% purity was used as the carrier gas. The substrate plate used was made of stainless steel 316L with dimensions of $90 \times 90 \times 6$ mm^3.

To define the best set of process parameters, that can ensure dense and crack free bulk samples, a multi-step approach was used (Fig. 4). First STs 30 mm in length were deposited with different laser power (P) and scan speed (v). Then, with optimized P and v, SLs (20×20 mm^2) were deposited to obtain the information about layer growth and penetration, so to define the layer thickness (Δz). Lastly, parallelepipeds of $20 \times 20 \times 15$ mm^3 were manufactured.

The process window for optimizing P and v was ranging from 500 to 900 W with step of 100 W and from 300 to 600 mm/min with step of 150 mm/min. The STs were deposited with a fixed powder feed rate (r) of 8 g/min, obtained using a rotation of powder feed motor of 6.0 rpm and a carrier gas flow rate (V_{ar}) of 5 L/min. To evaluate the different sets of P and v employed by OM, STs were cut perpendicular to scanning direction for obtaining cross-sections, as schematically shown in Fig. 5a. Characteristic geometrical features of cross-sections of STs such as width (W), total height (H), growth (G) and depth (D) were measured using the ImageJ software (Fig. 5b). The set of parameters with G/D ratio between 0.9 and 1.1 and with the lowest W/G ratio was selected to create single layers. The G/D ratio close to value 1.0 could mean having regular melt pool geometry and providing a good vertical metallurgical bonding without the risk of keyhole porosity. On the other hand, high G/D values would result in insufficient bonding between deposited layers, eventually leading to the balling effect geometry. While low G/D values would lead to keyhole geometry melt pools, therefore causing the risk of keyhole porosity. The other criteria

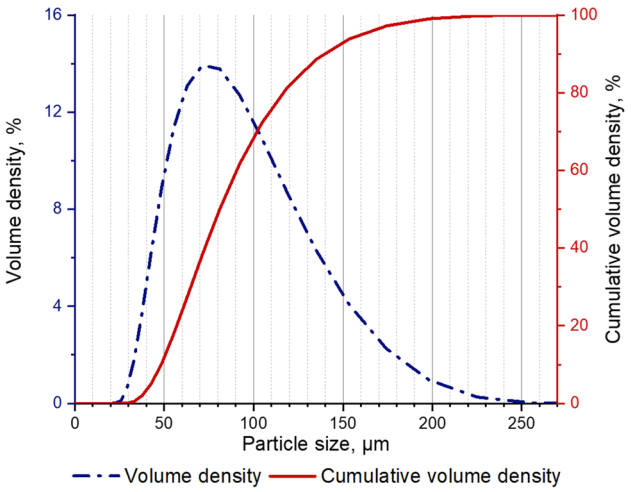

Fig. 1 W360 powder particle size distributions in the as received condition: the dotted blue curve corresponds to the distribution in volume, while the red curve to the cumulative volume distribution

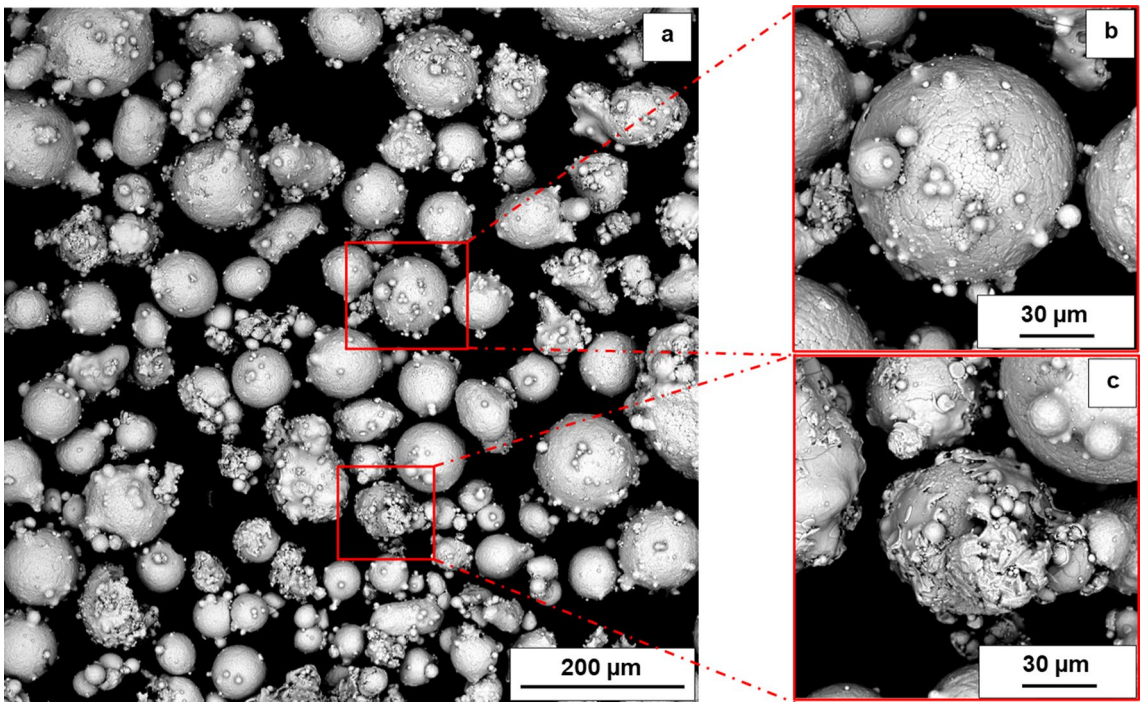

Fig. 2 SEM micrographs of **a** W360 powder in the as received condition, and magnifications showing **b** a particle with smaller satellites, **c** an agglomerated powder particle

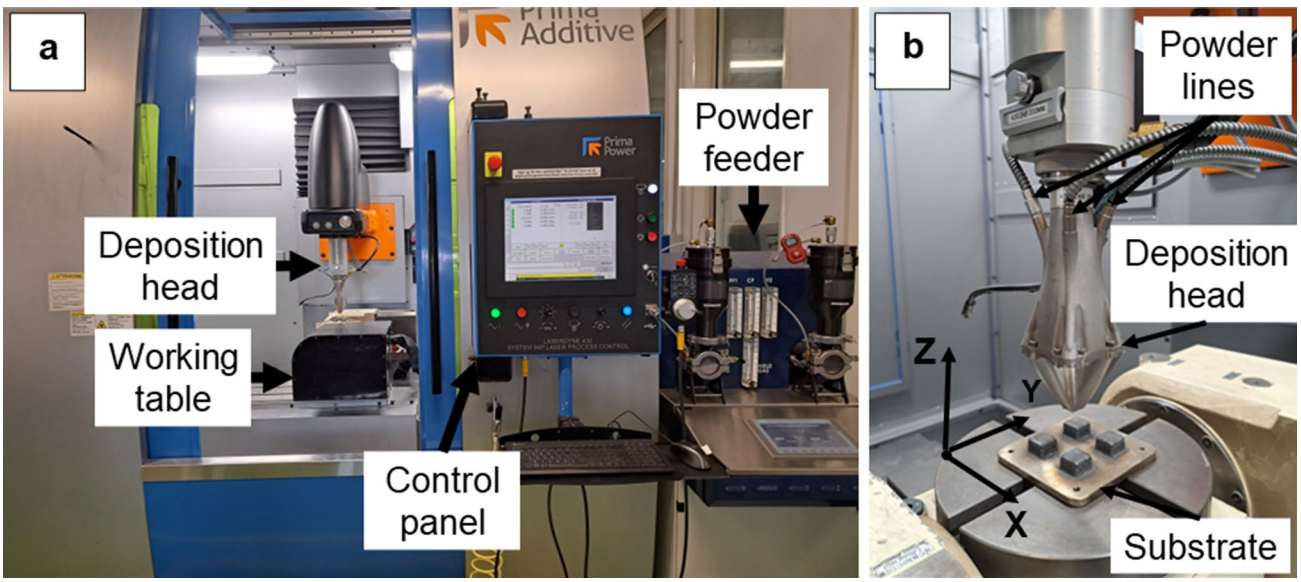

Fig. 3 Laserdyne 430 by Prima Additive: **a** picture of building chaimer, control panel and powder feeder, **b** picture of deposition head and working table with bulid parallelepiped samples

considered was the W/G ratio also called the aspect ratio: the lowest values are related to the highest growth of the samples [12].

Once defined the main process parameters (P and v, being r and V_{Ar} constant), five SLs with 40% pass overlapping (Ov) among each track, based on previous experience for a uniform layer growth, were deposited. They were fundamental to determine the layer thickness, also called

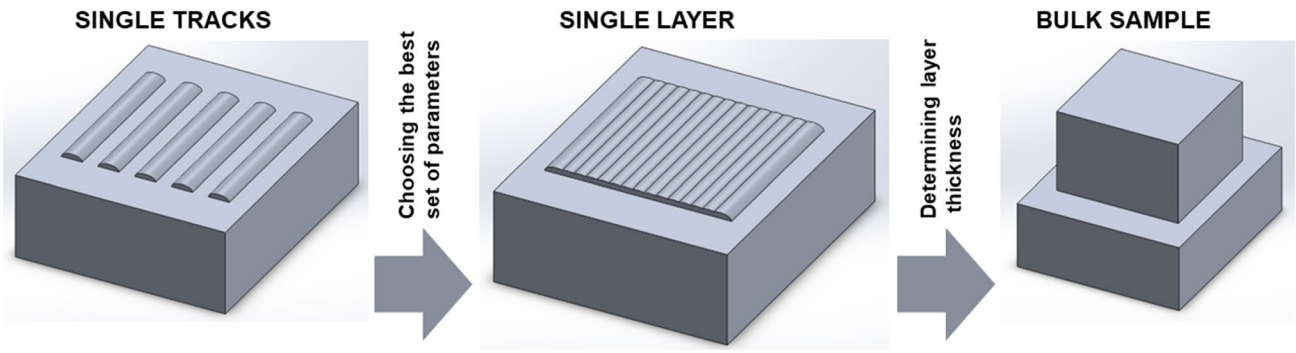

Fig. 4 Schematic explanation of the deposition procedure used in the present study and defined in a previous one [49]

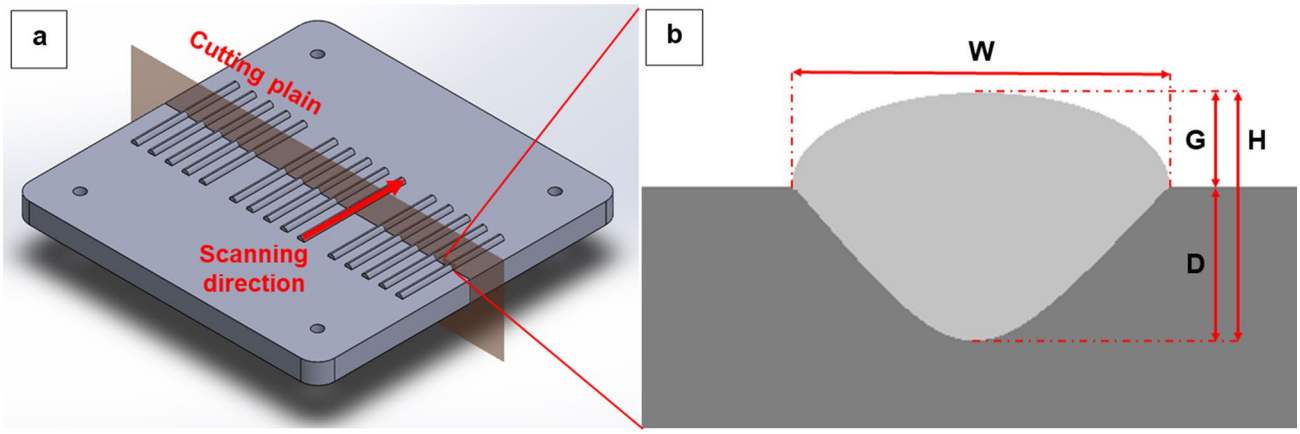

Fig. 5 Schematical view of **a** cut performed to analyse the single tracks deposited and **b** geometrical features of a ST cross-section considered as reference

z-step (Δz) for bulk sample deposition. A digital calliper TESA Micromaster with precision ± 0.004 mm was used to measure the thickness of the deposited SLs. Finally, six bulk parallelepipeds samples 20 × 20 × 15 mm^3 were deposited. The scanning strategy adopted was made by simple zigzag scanning pattern and a 90° rotation among consecutive layers.

Then the six parallelepiped samples were removed from substrate using wire electrical discharge machining. Two samples labelled AB were analysed without post processing in an as-built condition. Other samples were heat treated in tubular furnace (Nabertherm RHTC 80–710/15) with Ar-protected atmosphere following different steps as displayed in Fig. 6. The first heating to austenitizing temperature was done in three steps. A first step to 650 °C in 90 min followed by a isothermal for 15 min. A second step from 650 to 815 °C in 90 min followed by a isothermal for 30 min. The third step from 815 to 1050 °C in 120 min followed by a isothermal for 30 min. Samples were then quenched using a compressed air and two of them, labelled Q, were considered for microstructural analysis. After that, three consecutive tempering cycles were performed on the last two samples labelled HT. Each tempering cycle includes heating from room temperature to 540 °C in 10 min, holding at 540 °C for 60 min and air cooling [37].

2.3 Microstructural and Mechanical Characterization

All the bulk samples were cut in half along the build direction (also called *z-axis*). The obtained cross-sections were grinded and polished using a standard metallographic procedure for obtaining mirror like surface. The density, or the residual porosity, and the possible presence of cracks, were evaluated by analysing 25 optical micrographs taken at 100 × magnification for each sample using ImageJ software. Then the polished surfaces were etched with 2% Nital by immersion for 60 s for microstructural observations. They were carried out on etched cross-sections using the optical microscope LEICA DMI 5000 M and the Zeiss Supra TM 40 Field Emission Scanning Electron Microscope (FESEM). The compositional analysis was

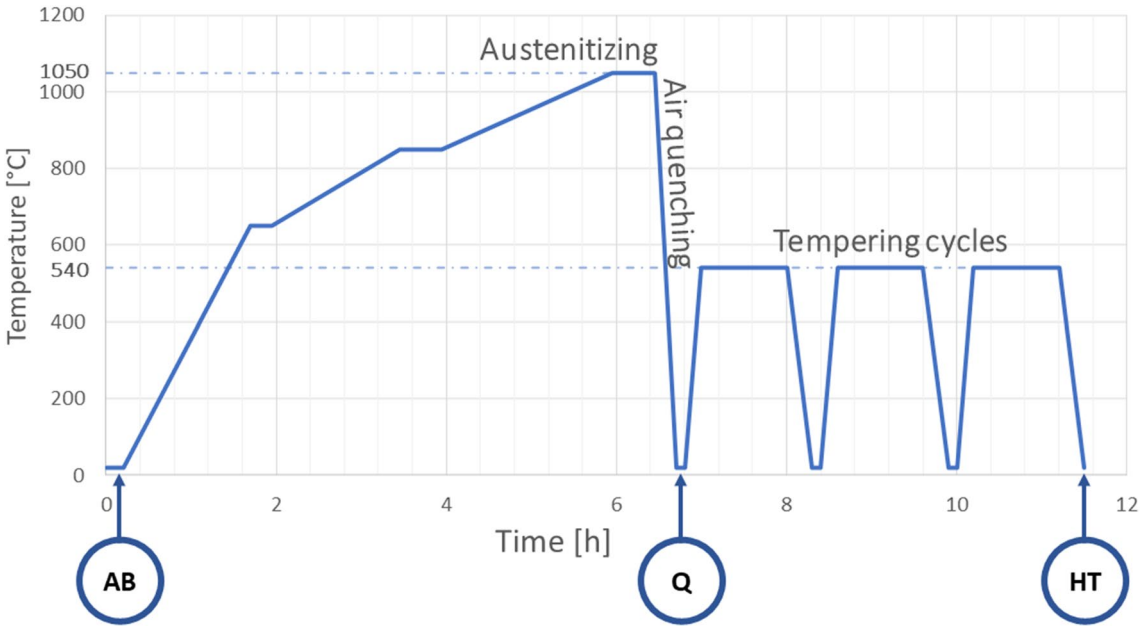

Fig. 6 The complete heat treatment performed on W360 samples: diagram with indication of sample condition in each step considered for characterization

Table 2 Main process parameters optimized to manufacture bulk samples in W360 steel by L-DED

P [W]	v [mm/min]	r [rpm]	V_{Ar} [L/min]	d_l [mm]	Ov [%]	Δz [mm]
800	450	6	5	2	40.0	0.65

conducted by Scanning Electron Microscope (SEM) EVO 15 equipped with an Energy-dispersive X-ray spectroscopy (EDX) detector.

The phase composition of samples in the cross section was analysed by X-ray diffraction (XRD) by using an Empyrean diffractometer (Cu Kα) in a Bragg Brentano configuration in a 2θ from 30 to 110°, operated at 40 kV and 40 mA with a step size 0.013 and 30 s per step.

DSC was carried out using Setaram TGA–DSC 92 16.18 in Argon atmosphere to avoid oxidation. The mass of the specimen, cut from the cylinder, was around 200 mg. Specimens were heated from 200 to 1120 °C with a heating rate 10 °C/min and subsequently cooled down to room temperature.

Micro-hardness was evaluated on bulk samples using a micro-Vickers indenter with a load of 500 g applied for 15 s. Five indentations were made "in line" as illustrated in Fig. 7 in five different zones on each sample at different height with respect to the substrate: bottom (B), central-bottom (CB), central (C), central-top (CT), and top (T) zones.

3 Results and Discussion

3.1 Definition of the L-DED Main Process Parameters

As stated before, the combination of P, v, and powder feed is crucial in L-DED for having a good metallurgical bonding between layers, a controlled layer growth and crack and pore free samples. Therefore, the evaluation of the cross-section

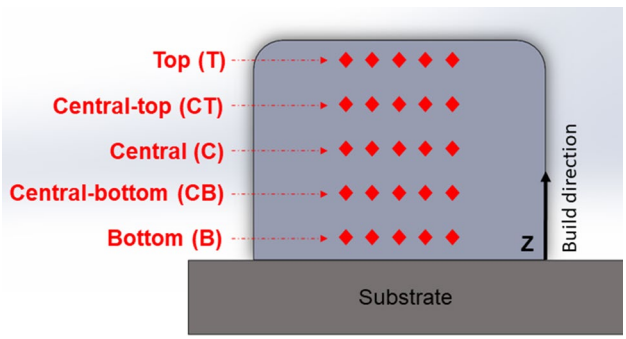

Fig. 7 Schematic representation of microhardness measurements with reported zones of sampling along building direction

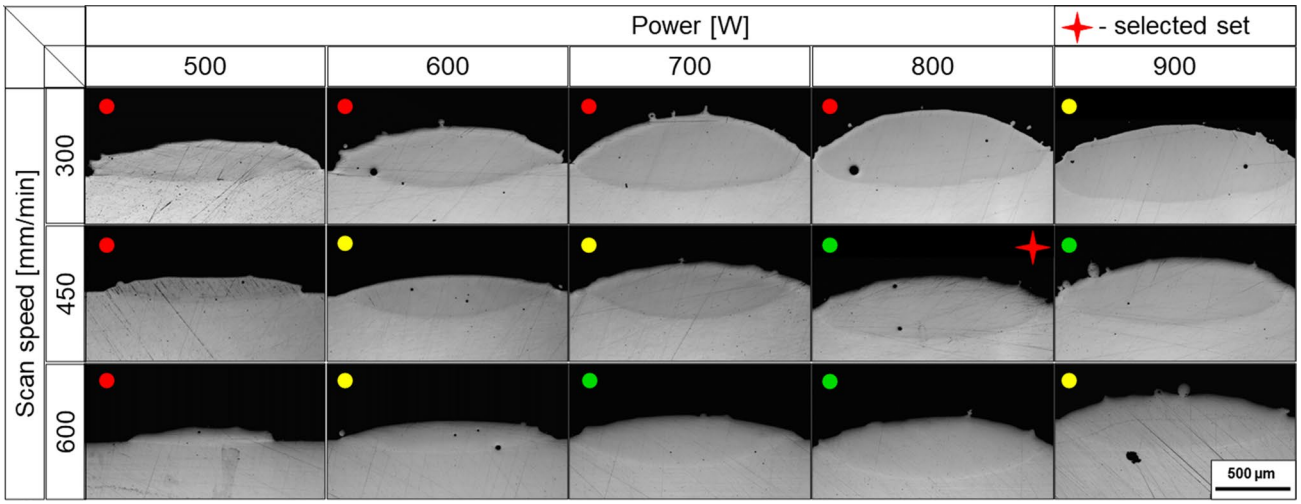

Fig. 8 Optical micrographs of cross-sections of the W360 STs produced with coloured marks corresponding to criteria defined in legenda of the diagram of Fig. 9

Table 3 EDX spot analysis with main alloying elements in % wt. of W360 by L-DED samples in AB, Q, and HT conditions. The spot number is related to Fig. 12

Spot	Description	Fe	Mo	Cr	V
1	Carbide – AB	69.3	5.8	5.3	0.9
2	Cell boundary – AB	85.6	3.3	4.8	0.6
3	Cell – AB	87.9	2.5	4.2	0.5
4	Carbide – Q	51.0	21.1	6.7	3.8
5	Martensite – Q	87.1	2.6	4.2	0.4
6	Carbide – HT	74.9	8.9	4.2	0.7
7	Tempered martensite – HT	86.2	2.5	4.3	0.5

optical micrographs of the STs made in W360 steel for different combinations of P and v was performed, and the results are summarized in Fig. 8 and in the diagram of Fig. 9. As can be seen from the cross sections of Fig. 8, it is possible to state that STs with the lowest P had a flat melt pool without penetration in the substrate, while STs with the lowest scan speed had higher growth than penetration, resulting in G/D values over 1.25 which could mean a bad metallurgical bonding between consecutive layers. By further analysis, STs with pair of parameters 600 W–450 mm/min and 600 W–600 mm/min had G/D values more acceptable with the criteria established and defined in the legenda of Fig. 9, but the corresponding W/G values were 12.54 and 12.28 respectively, indicating low growth of the STs. Considering STs with a P in the range 700 to 900 W and with v in the range 450 and 600 mm/min, it could be stated that they are in a good interval. In particular, the ST with combination of 800 W and 450 mm/min (marked with a red star in Fig. 8) had the G/D value closest to 1, which matches to a regular melt pool geometry. Furthermore, the corresponding W/G ratio

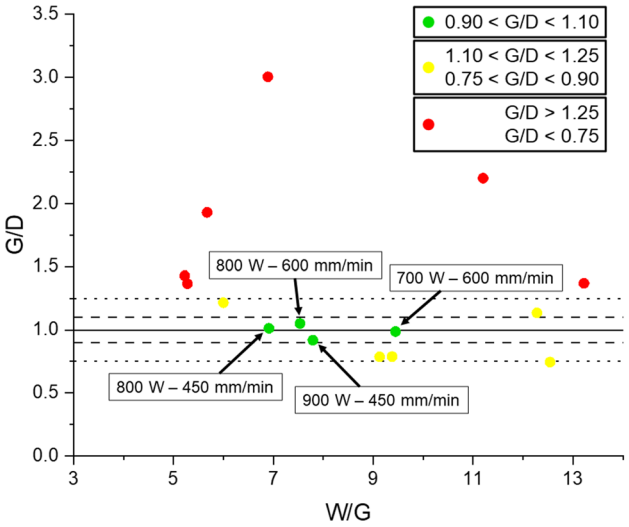

Fig. 9 Diagram summarizing the G/D ratio over W/G ratio (aspect ratio) with selection criteria lines

value was the lowest among the STs with the G/D values between 0.9 and 1.1 values. Therefore, it was defined as the P–v combination for W360 steel further SLs and bulk samples depositions.

Moreover, according to the width of the STs obtained with this P–v pair, and to the value Ov of 40%, the hatch distance (h_d) value to be set for SLs was of 1.2 mm. After that, the mean value of the growth of the five SLs built was measured. The result was 0.65 mm, and it was adopted as the Δz for manufacturing the parallelepiped bulk samples. The process parameters defined for processing the W360 steel by L-DED are summarized in Table 2.

All the samples produced had a measured mean density above 99.8%, with mean residual porosity value of 0.15%. The pores found in the samples were spherical gas pores that are typical for the L-DED process due to the fact that inert gases are used for delivering powder to the melt pool and for shielding the melt pool in order to prevent oxidation. Moreover, no cracks were found despite its high carbon equivalent content value of 2.15% calculated with Eq. (1). This can be explained considering that the L-DED process has lower cooling rates and a different thermal history compared to the L-PBF process: a higher energy source is employed, with a larger laser spot size, with a nominal diameter one order of magnitude greater, and with lower scan speed [25, 32].

3.2 Microstructural Analysis

The samples microstructure was investigated with optical and SEM microscopes. The optical micrographs of the AB, Q and HT samples at different magnifications are shown in Fig. 10. From the microstructure of the AB sample presented in Fig. 10a, the characteristic L-DED microstructure can be observed, consisting of interconnected melt pools and a dendritic-cellular microstructure with both equiaxed and columnar dendrites. At higher magnification (Fig. 10b), cells, intercellular white phase, very fine carbides in shape of black dots can be detected. As discussed in previous studies [14, 19, 50] the microstructure of similar as-built hot work tool steels, such as H13, exhibits a dendritic-cellular structure with intercellular micro-segregation of the alloying elements, suggesting the presence of retained austenite. It should be noted that carbide particles (marked by red arrows) were found only within the intercellular areas. The Q sample (Fig. 10c and d) exhibits the typical microstructure of quenched hot work tool steels, characterized by numerous small martensite laths and carbides. Moreover, the comparison with the AB state indicates that after the austenitizing heat treatment, the melt pools and the dendritic-cellular microstructure are no longer visible, indicating also that this heat treatment is sufficient to modify the effects of the complex thermal history to which the material was subjected. The resulting microstructure is more homogenized, with the recovery of micro-segregated elements from the cell boundaries and partial dissolution of the carbides through a diffusional process facilitated by the austenitizing heat treatment. In the HT sample (Fig. 10e and f) the microstructure is homogeneous, consisting of tempered martensite and a great quantity of carbides. To gain a better understanding of the microstructural features observed in Fig. 10, an investigation through FESEM was performed and the most representative micrographs of the three conditions are shown in Fig. 11.

In particular, Fig. 11a shows the dendritic-cellular microstructure of the AB sample, the light grey phase corresponds to tempered martensite within cells, while the darker grey phase is the intercellular region suspected to be retained austenite. At higher magnification (Fig. 11b), very fine carbides (marked with red arrows) can be observed in the intercellular area, which exhibits a distinct microstructure compared to the cellular phase. The presence of intercellular carbides is consistent with findings from other studies on H13, a similar hot work tool steel [14]. In the Q condition (Fig. 11c and d), the austenite phase has transformed into a martensitic microstructure [51]. Moreover, in this sample, the dendritic-cellular microstructure typically observed in L-DED samples has disappeared, likely due to the reaching of the austenitizing temperature. With increased magnification, larger carbides can also be observed (Fig. 11d). In HT condition, as shown in Fig. 11e and f, the characteristic microstructure of tempered hot work tool steels is evident [52]. The growth of martensite laths and carbides can be observed, whit the carbides appearing larger in size and number compared to the AB and Q samples.

To better understand the composition of the matrix and of the carbides, EDX point analyses were performed. The results in terms of % in weight of Fe, Mo, Cr, and V of the analysis for the AB, Q, and HT samples are presented in Table 3, and the corresponding points are shown in the SEM micrographs reported in Fig. 12. The Si and Mn results are not included in table as they are not relevant for carbide analysis.

It should also be noted that the EDX sensor used was incapable of accurately measuring the C content, hence no results are provided for C. In the micrograph of the AB sample (Fig. 12a), a noticeable difference in microstructure between the cell and the cell boundary is evident. Additionally, white spots representing carbides are observed only at the cell boundary. Comparing the EDX point analysis results for spots 1, 2, and 3 (Table 2), it can be observed that the weight percentage of alloying elements Mo, Cr, and V is slightly higher in the cell boundary (spot 2) than in the cell (spot 3), confirming the micro-segregation of alloying elements reported in previous studies [19, 50]. Moreover, the EDX spot analysis reveals an increase in the carbide-forming elements in the carbides. Notably, Mo exhibits the most significant increase, with its content rising from 2.5% wt. in the cell (spot 4) to 3.3% in the cell boundary (spot 3), and reaching a value of 5.8% in the carbide (spot 1).

Analysing the Q sample, the EDX spot analysis (Fig. 12b) indicates a homogenized martensitic matrix (spot 5), resulting from the diffusion-based homogenization during the austenitization phase at high temperature, as observed by Amirabdollahian et al. on H13 by L-DED [14]. Furthermore, some carbides in the Q sample exhibit increased content of all measured alloying elements (spot 4) compared to the carbide in the AB sample (spot 1). Specifically, Mo content increased from 5.8 to 21.1%, Cr content increased from 5.3 to 6.7%, and V content increased from 0.9 to 3.8%.

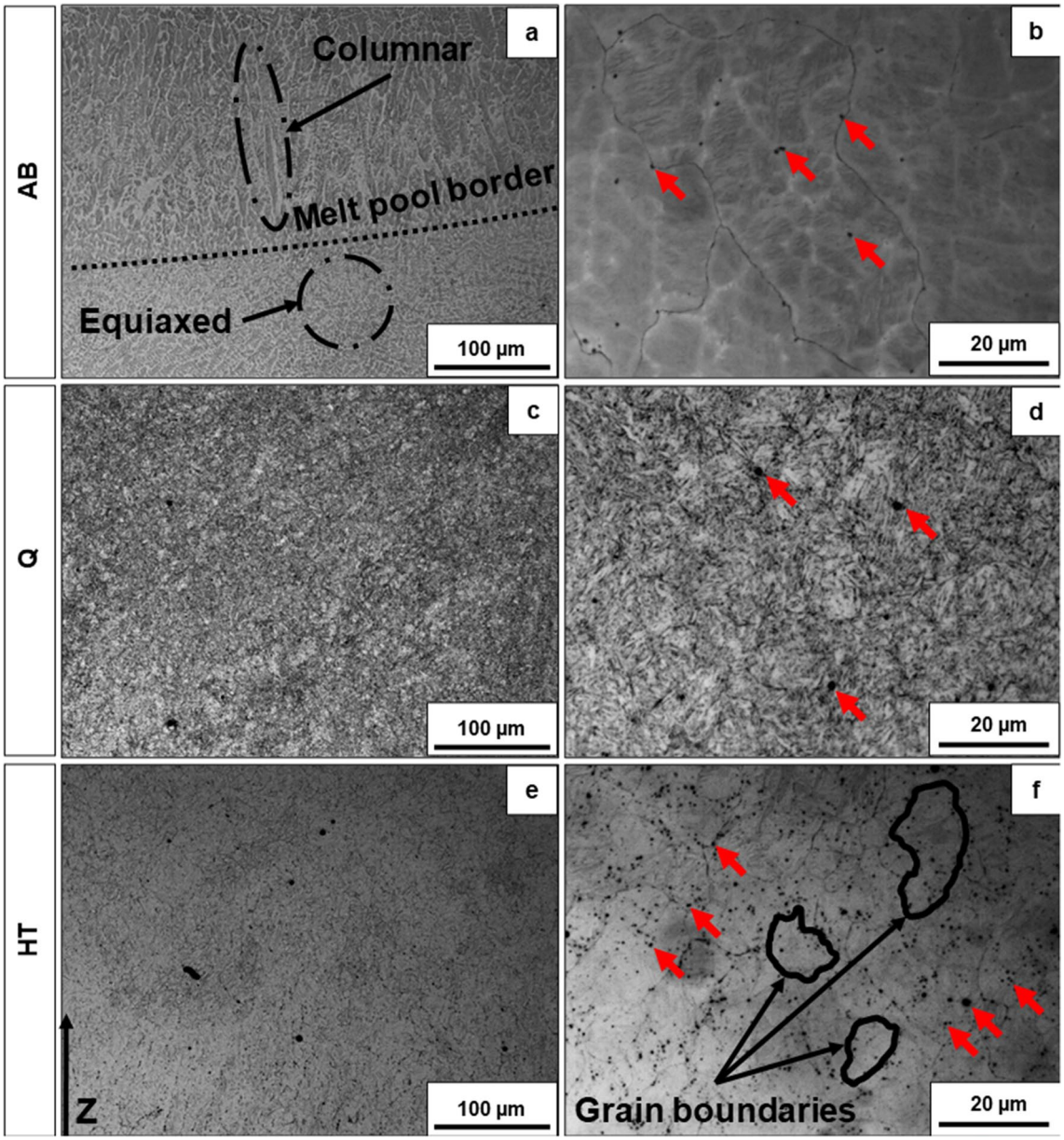

Fig. 10 Optical micrographs of W360 AB (**a**, **d**), Q (**b**, **e**) and HT (**c**, **f**) samples at different magnifications

In the HT sample, the tempering process had no significant impact on the change in alloying element content in the matrix. The tempered martensite (spot 7) exhibited similar alloying element content as the as-quenched martensite (spot 5). Additionally, the carbide (spot 6) in the HT sample showed that the content of Cr remained at a similar level as in the matrix (spot 7), being 4.2% in the carbide and 4.3% in the matrix. Moreover, the amount of V slightly increased from 0.5% in the matrix to 0.7% in the carbide. Meanwhile, the content of Mo increased from 2.5 to 8.9%, indicating that there are mainly Mo-rich carbides, which is consistent with the findings of Amirarsalani et al. [53].

To summarize the EDX analysis, the carbides in the AB sample underwent intrinsic tempering, which was not controlled like the tempering process in the HT sample. This suggests that the carbides in the AB sample were tempered at different temperatures, ranging from high to low, as the deposition process progressed [17]. This phenomenon of intrinsic tempering occurred at different stages, promoting the growth of different carbide types. It could be stated that at temperatures around 650 °C, the growth of V carbides was primarily encouraged, while at temperatures between 538 and 592 °C, the growth of Mo carbides was favoured. Finally, at temperatures around 427 °C, the promotion of Cr carbides became

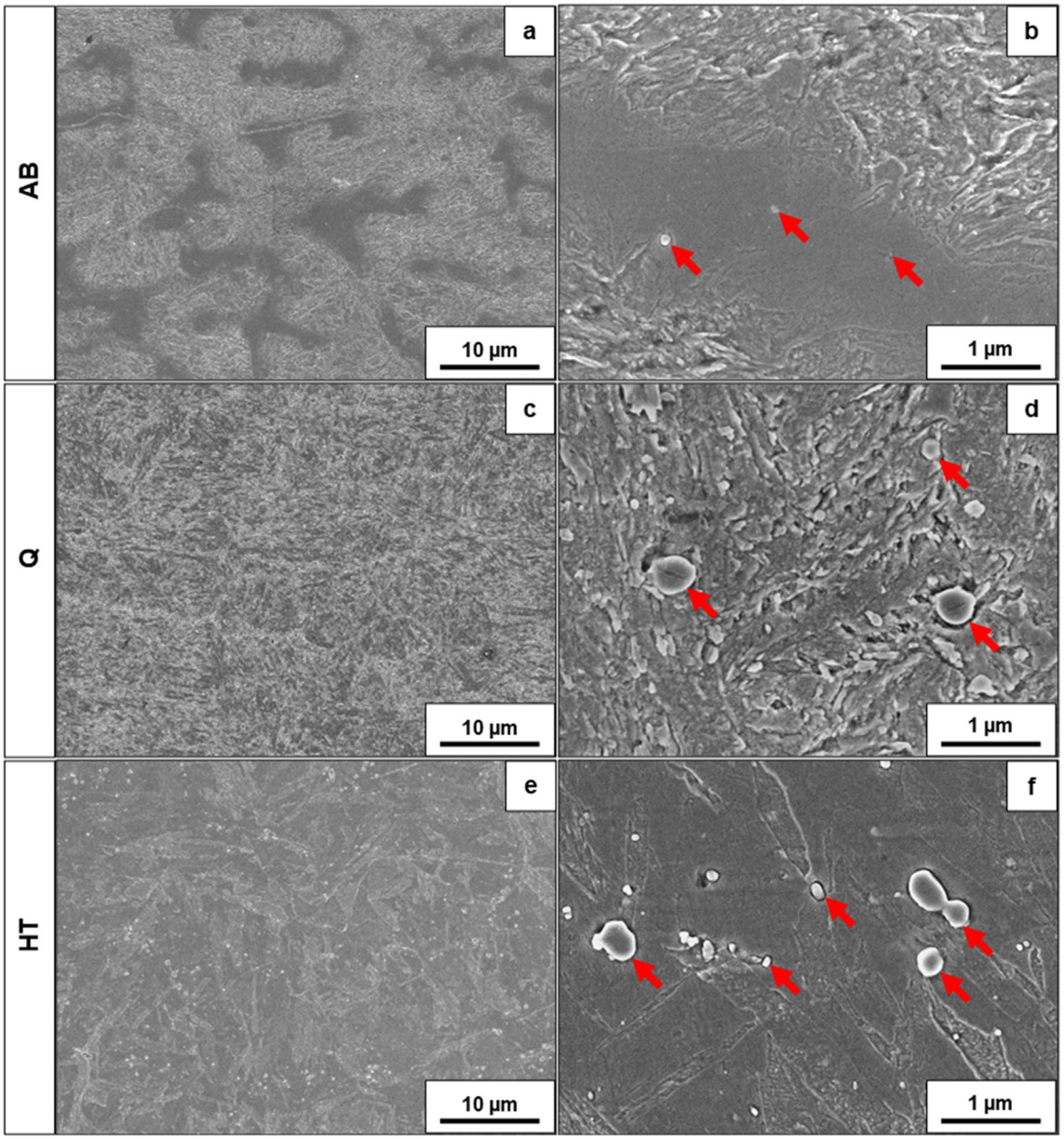

Fig. 11 FESEM micrographs of revealed microstructure of AB (**a**, **d**), Q (**b**, **e**) and HT (**c**, **f**) samples at different magnifications

significant [54]. This could explain the increase in the content of all carbide-forming elements in the spot analyses corresponding to the carbides of the AB sample. In contrast, it can be supposed that the HT sample underwent controlled tempering at 540 °C, which predominantly promoted the growth of Mo-rich carbides [54]. Furthermore, in the HT sample, the content of Cr did not increase in relation to the martensitic matrix, perhaps indicating that its role in W360 steel is mainly to stabilize martensite [52].

Subsequently, XRD measurements were conducted to validate the hypotheses presented in Figs. 10 and 11 regarding the detected phases (Fig. 13). The XRD patterns of the AB, Q, and HT samples all exhibited the peaks corresponding to martensitic phase.

The peak values reported in Fig. 13a correspond to the body-centered cubic (BCC) system C free steel structure. It is well-known that the martensite lattice parameter changes with the increase of C content into the lattice [55]. In the reflection magnification of Fig. 13b the shift of the first peak of all patterns compared to the α (110) value can be observed. It could be explained with the fact that through the rapid cooling from the austenitizing temperature, the C gets trapped in the BCC lattice causing the change of lattice parameters. During tempering the C diffuses out of

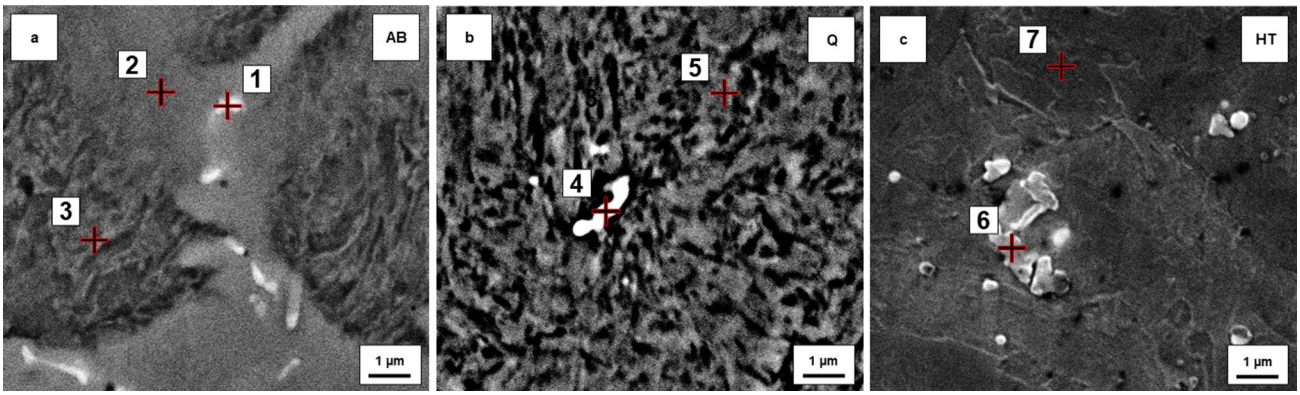

Fig. 12 SEM micrographs used for EDX spot analysis **a** of AB sample, **b** of Q sample, **c** of HT sample

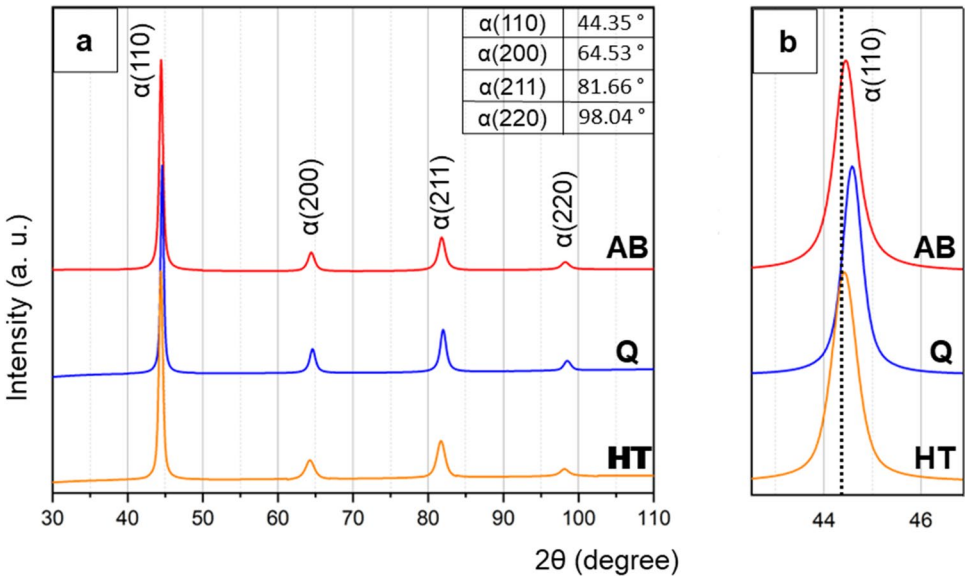

Fig. 13 XRD patterns of **a** AB, Q and HT samples with reported α values; **b** a magnification of the first peak for the *α* (110) value in AB, Q and HT samples in comparison to the theoretical one (dotted line)

the lattice, therefore bringing back the peak related to the lattice parameters. The C diffusion promotes the formation and growth of carbides. However it should be noted that, although carbides are certainly present, their content and the content of retained austenite, if present, is less than 4% of the volume content, thus they were not detected by XRD analysis. However, the presence of different carbides content could be assessed by means of DSC analyses.

Performing the DSC measurements, two endothermic peaks were found clearly in the thermograms for all the bulk samples (Fig. 14). They were labelled as Peak 2 and Peak 3. While in Q samples it was found also an exothermic event that occurs between 500 and 600 °C. This is probably due to the Mo carbide formation since it is reported in literature that they could form easily between 538 and 592 °C [54]. Peak 1 was not detected in HT samples because the carbides were already formed, while in the AB samples, as already stated before, an intrinsic tempering occurred during the L-DED process resulting in the carbide formation and growth. The first endothermic event, peak 2 is the Curie temperature (T_C) that is related to the magnetic transformation, it appears at 770 °C for Q and HT samples, while for the AB sample the peak is shifted to the right at 779 °C [56]. The peak 3 is associated to the transformation from α to γ. Austenite onset temperature (AC_1) for all three samples was measured to be 839 °C. On the other hand, austenite finish temperature (AC_3) was at 874 °C for Q and HT samples, while for AB sample was found at 882 °C. The peaks shift to the right of the T_c and AC_3 temperatures could be explained by the difference in the grain sizes. In the optical micrographs of AB and HT samples (Fig. 10b and f) it is possible to see such differences between the grain sizes. The transformation from martensite to austenite is starting at the grain boundaries and therefore smaller grain sizes are being transformed faster. As reported in literature for H13 tool steel, using the same heating rate in DSC measurements,

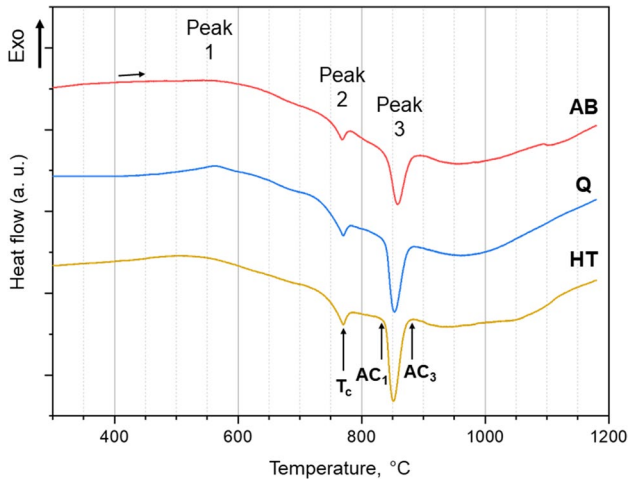

Fig. 14 Heating DSC curves of the AB, Q and HT samples

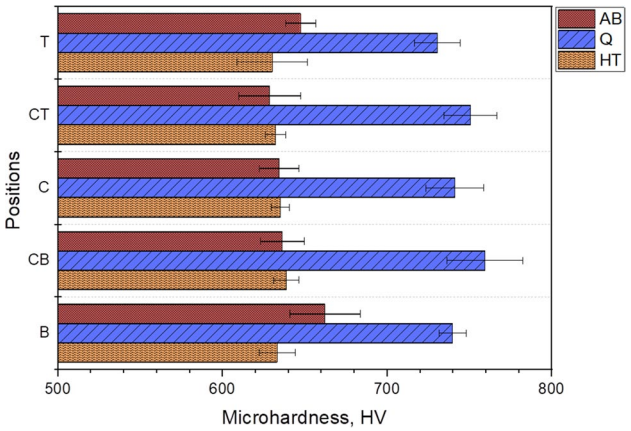

Fig. 15 Microhardness mean values for AB, Q and HT W360 samples reported for different positions along building direction

the larger grain size condition was having higher AC_3 temperature, in our case AB samples [57, 58].

Finally, the effects of these microstructural features on the materials properties were evaluated trough hardness tests. In Fig. 15 the microhardness mean values of AB, Q and HT W360 steel samples are displayed following an order related to the positions where measurements were performed, along the height of the cross section of the samples starting from the substrate, hence along the build direction (as indicated in Fig. 7).

The AB sample hardness showed a certain trend along the building direction. The bottom of the sample had measured the highest values, the microhardness is decreasing with upper layers until the top part of the sample where an increase in microhardness was noted. This trend could be explained with the fact that temperatures of the substrate were increasing with more layers added which is resulting in slower cooling rates, therefore lower microhardness values. While the increased value of the top of the AB sample could be due to not having upper layers deposited on top that would hold the layer at elevated temperatures for longer time and thus have the tempering effect on it. The trend found in the AB condition was not found in the Q and HT samples, suggesting that the thermal history can be erased by the heat treatment performed. The mean value of AB samples was 642 while, showing that as quenched, Q sample has as expected the highest microhardness value of 744 HV due to the highest internal stress present which makes it more brittle. Moreover, while reducing the risk of cracks with three tempering cycles the value of HT samples microhardness dropped to 634 HV which is the expected hardness for the performed heat treatment and suitable for tools repair applications [37].

4 Conclusions

In this work, the processability of W360 tool steel by L-DED was demonstrated for the first time. A fast approach for optimizing process parameters was adopted, starting with the deposition and analyses of single tracks (STs) and single layers (SLs). Bulk samples were obtained and characterized in terms of microstructure and microhardness at different conditions: as built (AB), after austenitizing and air quenching (Q), and after three consecutive tempering cycles (HT). The main findings of this study are summarized below:

(1) Once a powder feed rate of 8 g/min was fixed, the best combination of laser power and scan speed was determined to be 800 W and 450 mm/min through STs analyses. An overlapping of 40% among consecutive scan tracks was chosen, and a hatching distance of 1.2 mm was defined for the SLs. After deposition and measurement, a layer thickness of 0.65 mm was defined. Lastly, a zig-zag pattern with 90° rotation among consecutive layers was adopted as the scanning strategy. The L-DED samples of W360 steel resulted in bulk crack-free samples with a mean relative density above 99.8%.

(2) Microstructural analysis of the AB samples revealed the characteristic L-DED microstructure of W360 steel, consisting of a dendritic-cellular microstructure with both equiaxed and columnar dendrites. The presence of very fine carbides in the intercellular regions was also observed. The Q samples exhibited numerous small martensite laths and an increased presence of carbides, which were also larger in size compared to the AB samples. Subsequent tempering cycles resulted in a homogeneous microstructure of tempered martensite with an even greater quantity of carbides.

(3) EDX point analyses provided semi-quantitative information about the chemical composition of the matrix and car-

bides in the AB, Q and HT samples. Variations in weight percentage of the main alloying elements Fe, Mo, Cr, and V content were observed among the different microstructural conditions. Micro-segregation of alloying elements in the cell boundary was observed in the AB samples. Furthermore, the carbides were found to be mostly Mo-rich carbides.

(4) XRD results showed only the presence of the martensite phase in all conditions, with no retained austenite or carbide peaks observed.

(5) DSC analysis showed an exothermic peak only in Q sample, while the AB and HT samples exhibited similar trends, probably due to the intrinsic heat treatment of the AB sample during the deposition process and the tempering cycles performed in the HT sample.

(6) The microhardness tests revealed a certain trend in the AB samples along the building direction (*z-axis*), which is characteristic of steels processed by L-DED due to deposition on a cold substrate and intrinsic thermal treatment. The first and last layers deposited showed higher hardness values (662 HV and 647 HV, respectively), while the middle layers exhibited lower hardness (633 HV). The Q samples exhibited the highest mean hardness values, which are expected to correspond to the condition with the highest residual thermal stresses. After the HT, a mean hardness value of 634 HV was measured, which remained constant along the building direction, confirming the homogeneous microstructure obtained after preformed heat treatment.

In conclusion, the results suggest that W360 steel has great potential for various applications enabled by additive manufacturing (AM) and in particular by L-DED, including the production of complex components with internal cooling channels, and mould and tool repair. Further analyses, such as tensile testing and wear resistance evaluation, can be conducted to fully assess the mechanical properties and performance of W360 L-DED samples in specific industrial applications. Additionally, investigating different post-heat treatment to fine-tune the microstructural properties of W360 steel could further enhance its mechanical properties.

Acknowledgements The authors would like to acknowledge the regional project “4 ASSI—4 Assi Assieme per innovare”, funded by Regione Piemonte with Grant POR FESR Piemonte 2014-2020 Piattaforma tecnologica di “Bando PiTeF”.

Author contributions All authors contributed to the study conception and design. Material preparation, data collection and analysis were performed by JV, Alberta Aversa and DM. The first draft of the manuscript was written by JV, and all authors commented on previous versions of the manuscript. All authors read and approved the final manuscript.

Funding Open access funding provided by Politecnico di Torino within the CRUI-CARE Agreement.

Declarations

Conflict of interest The authors declare no conflict of interest.

References

1. T. Wohlers, T. Gornet, History of Additive Manufacturing (Wohlers Associate, Fort Collins, 2015). Available: https://wohlersassociates.com/wp-content/uploads/2022/08/history2015.pdf
2. https://mitsloan.mit.edu/ideas-made-to-matter/additive-manufacturing-explained. Accessed: 3 June 2023
3. R. Kawalkar, H.K. Dubey, S.P. Lokhande, A review for advancements in standardization for additive manufacturing. Mater. Today Proc. **50**, 1983–1990 (2022). https://doi.org/10.1016/j.matpr.2021.09.333
4. I. Gibson, D. Rosen, B. Stucker, M. Khorasani, *Additive Manufacturing Technologies* (Springer, Cham, 2021)
5. D.G. Ahn, Directed energy deposition (DED) process: state of the art. Int. J. Precision Eng. Manufact. Green Technol. **8**(2), 703–742 (2021). https://doi.org/10.1007/s40684-020-00302-7
6. S.L. Sing, C.F. Tey, J.H.K. Tan, S. Huang, W.Y. Yeong, 3D printing of metals in rapid prototyping of biomaterials: Techniques in additive manufacturing, in *Rapid Prototyping of Biomaterials*, 2nd edn., ed. by R. Narayan (Woodhead Publishing, Sawston, 2020), pp.17–40. https://doi.org/10.1016/B978-0-08-102663-2.00002-2
7. C.-J. Bae, A.B. Diggs, A. Ramachandran, Quantification and certification of additive manufacturing materials and processes, in *Additive Manufacturing: Materials, Processes, Quantifications and Applications*, ed. by J. Zhang, Y.-G. Jung (Butterworth-Heinemann, Oxford, 2018), pp.181–213. https://doi.org/10.1016/B978-0-12-812155-9.00006-2
8. N. Shamsaei, A. Yadollahi, L. Bian, S.M. Thompson, An overview of Direct Laser Deposition for additive manufacturing; Part II: mechanical behavior, process parameter optimization and control. Addit. Manuf. **8**, 12–35 (2015). https://doi.org/10.1016/j.addma.2015.07.002
9. E.M. Palmero, A. Bollero, 3D and 4D Printing of functional and smart composite materials, in *Encyclopedia of Materials: Composites* (Elsevier, Amsterdam, 2018), pp.402–419. https://doi.org/10.1016/B978-0-12-819724-0.00008-2
10. K. Munir, A. Biesiekierski, C. Wen, Y. Li, Powder metallurgy in manufacturing of medical devices, in *Metallic Biomaterials Processing and Medical Device Manufacturing*, ed. by C. Wen (Elsevier, 2020), pp.159–190. https://doi.org/10.1016/B978-0-08-102965-7.00005-9
11. J.M. Wilson, C. Piya, Y.C. Shin, F. Zhao, K. Ramani, Remanufacturing of turbine blades by laser direct deposition with its energy and environmental impact analysis. J. Clean. Prod. **80**, 170–178 (2014). https://doi.org/10.1016/j.jclepro.2014.05.084

12. E. Toyserkani, A. Khajepour, S.F. Corbin, *Laser Cladding* (CRC Press, Boca Raton, 2004). https://doi.org/10.1201/9781420039177
13. A. Saboori, A. Aversa, G. Marchese, S. Biamino, M. Lombardi, P. Fino, Application of directed energy deposition-based additive manufacturing in repair. Appl. Sci. **9**(16), 3316 (2019). https://doi.org/10.3390/app9163316
14. S. Amirabdollahian, F. Deirmina, M. Pellizzari, P. Bosetti, A. Molinari, Tempering behavior of a direct laser deposited hot work tool steel: Influence of quenching on secondary hardening and microstructure. Mater. Sci. Eng. A **814**, 141126 (2021). https://doi.org/10.1016/j.msea.2021.141126
15. E.B. Fonseca, J.D. Escobar, A.H.G. Gabriel, G.G. Ribamar, T. Boll, É.S.N. Lopes, Tempering of an additively manufactured microsegregated hot-work tool steel: a high-temperature synchrotron X-ray diffraction study. Addit. Manuf. **55**, 102812 (2022). https://doi.org/10.1016/j.addma.2022.102812
16. E.S. Kim, F. Haftlang, S.Y. Ahn, G.H. Gu, H.S. Kim, Effects of processing parameters and heat treatment on the microstructure and magnetic properties of the in-situ synthesized Fe-Ni permalloy produced using direct energy deposition. J. Alloys Compd. **907**, 164415 (2022). https://doi.org/10.1016/j.jallcom.2022.164415
17. J. Epp, J. Dong, H. Meyer, A. Bohlen, Analysis of cyclic phase transformations during additive manufacturing of hardenable tool steel by in-situ X-ray diffraction experiments. Scr. Mater. **177**, 27–31 (2020). https://doi.org/10.1016/j.scriptamat.2019.09.021
18. J. Mazumder, J. Choi, K. Nagarathnam, J. Koch, D. Hetzner, The direct metal deposition of H13 tool steel for 3-D components. JOM **49**(5), 55–60 (1997). https://doi.org/10.1007/BF02914687
19. F. Deirmina, N. Peghini, B. AlMangour, D. Grzesiak, M. Pellizzari, Heat treatment and properties of a hot work tool steel fabricated by additive manufacturing. Mater. Sci. Eng. A **753**, 109–121 (2019). https://doi.org/10.1016/j.msea.2019.03.027
20. X. Peng, L. Kong, J.Y.H. Fuh, H. Wang, A review of post-processing technologies in additive manufacturing. J. Manuf. Mater. Process. **5**(2), 38 (2021). https://doi.org/10.3390/jmmp5020038
21. M. Laleh, E. Sadeghi, R.I. Revilla, Q. Chao, N. Haghdadi, A.E. Hughes, W. Xu, I. De Graeve, M. Qian, I. Gibson, M.Y. Tan, Heat treatment for metal additive manufacturing. Prog. Mater. Sci. **133**, 101051 (2023). https://doi.org/10.1016/j.pmatsci.2022.101051
22. D. Svetlizky, M. Das, B. Zheng, A.L. Vyatskikh, S. Bose, A. Bandyopadhyay, J.M. Schoenung, E.J. Lavernia, N. Eliaz, Directed energy deposition (DED) additive manufacturing: physical characteristics, defects, challenges and applications. Mater. Today **49**, 271–295 (2021). https://doi.org/10.1016/j.mattod.2021.03.020
23. E.O. Olakanmi, R.F. Cochrane, K.W. Dalgarno, A review on selective laser sintering/melting (SLS/SLM) of aluminium alloy powders: Processing, microstructure, and properties. Prog. Mater. Sci. **74**, 401–477 (2015). https://doi.org/10.1016/j.pmatsci.2015.03.002
24. J. Leunda, C. Soriano, C. Sanz, V.G. Navas, Laser cladding of vanadium-carbide tool steels for die repair. Phys. Procedia **12**, 345–352 (2011). https://doi.org/10.1016/j.phpro.2011.03.044
25. G. Roberts, G. Krauss, R. Kennedy, *Tool Steels*, 5th edn. (ASM International, Almere, 1998)
26. R.P. Mudge, N.R. Wald, Laser engineered net shaping advances additive manufacturing and repair. Weld. J.-New York **86**(1), 44 (2007)
27. P. Bajaj, A. Hariharan, A. Kini, P. Kürnsteiner, D. Raabe, E.A. Jägle, Steels in additive manufacturing: a review of their microstructure and properties. Mater. Sci. Eng. A **772**, 138633 (2020). https://doi.org/10.1016/j.msea.2019.138633
28. R.W. Hinton, R.K. Wiswesser, Estimating welding preheat requirements for unknown grades of carbon and low-alloy steels. Weld J. **87**(11), 273–276 (2008)
29. M. Bruneau, U. Chia-Ming, R. Sabelli, *Ductile Design of Steel Structures*, 2nd edn. (McGraw-Hill Education, New York, 2011)
30. J. Krell, A. Röttger, K. Geenen, W. Theisen, General investigations on processing tool steel X40CrMoV5-1 with selective laser melting. J Mater. Process. Technol. **255**, 679–688 (2018). https://doi.org/10.1016/j.jmatprotec.2018.01.012
31. O.S. Odebiyi, S.M. Adedayo, L.A. Tunji, M.O. Onuorah, A review of weldability of carbon steel in arc-based welding processes. Cogent Eng. **6**(1), 609180 (2019). https://doi.org/10.1080/23311916.2019.1609180
32. J. Boes, A. Röttger, C. Mutke, C. Escher, S. Weber, Microstructure and properties of a novel carbon-martensitic hot work tool steel processed by laser additive manufacturing without preheating. Steel Res. Int. **94**(4), 2200439 (2023). https://doi.org/10.1002/srin.202200439
33. P.M. Novotny, M.K. Banerjee, Tool and Die Steels, in *Reference Module in Materials Science and Materials Engineering*. (Elsevier, Amsterdam, 2016). https://doi.org/10.1016/B978-0-12-803581-8.02534-0
34. A.J. Pinkerton, L. Li, Direct additive laser manufacturing using gas- and water-atomised H13 tool steel powders. Int. J. Adv. Manufact. Technol. **25**(5–6), 471–479 (2005). https://doi.org/10.1007/s00170-003-1844-2
35. C.D. Naiju, P.M. Anil, Influence of operating parameters on the reciprocating sliding wear of direct metal deposition (DMD) components using Taguchi method. Procedia Eng. **174**, 1016–1027 (2017). https://doi.org/10.1016/j.proeng.2017.01.254
36. D. Svetlizky et al., Laser-based directed energy deposition (DED-LB) of advanced materials. Mater. Sci. Eng. A **840**, 142967 (2022). https://doi.org/10.1016/j.msea.2022.142967
37. Heat Treatment Guidelines - Bohler W360 Isobloc (2017). Available: http://www.sayaht.com/pdf/BOHLER-W360-ISOBLOC-htr.pdf. Accessed: 16 Sep. 2022
38. J. Mazumder, A. Schifferer, J. Choi, Direct materials deposition: designed macro and microstructure. Mater. Res. Innov. **3**(3), 118–131 (1999). https://doi.org/10.1007/s100190050137
39. R. Cottam, J. Wang, V. Luzin, Characterization of microstructure and residual stress in a 3D H13 tool steel component produced by additive manufacturing. J. Mater. Res. **29**(17), 1978–1986 (2014). https://doi.org/10.1557/jmr.2014.190
40. R.T. Jardin et al., Sensitivity analysis in the modelling of a high speed steel thin-wall produced by directed energy deposition. Metals (Basel) **10**(11), 1554 (2020). https://doi.org/10.3390/met10111554
41. G.Y. Baek et al., Mechanical characteristics of a tool steel layer deposited by using direct energy deposition. Met. Mater. Int. **23**(4), 770–777 (2017). https://doi.org/10.1007/s12540-017-6442-1
42. S.M.T. Omar, K.P. Plucknett, The influence of DED process parameters and heat-treatment cycle on the microstructure and hardness of AISI D2 tool steel. J. Manuf. Process. **81**, 655–671 (2022). https://doi.org/10.1016/j.jmapro.2022.06.069
43. L. Xue, J. Chen, S.-H. Wang, Freeform laser consolidated H13 and CPM 9V tool steels. Metallogr. Microstruct. Anal. **2**(2), 67–78 (2013). https://doi.org/10.1007/s13632-013-0061-0
44. P. Kattire, S. Paul, R. Singh, W. Yan, Experimental characterization of laser cladding of CPM 9V on H13 tool steel for die repair applications. J. Manuf. Process. **20**, 492–499 (2015). https://doi.org/10.1016/j.jmapro.2015.06.018
45. L.P. Borrego, J.T.B. Pires, J.M. Costa, J.M. Ferreira, Mould steels repaired by laser welding. Eng. Fail. Anal. **16**(2), 596–607 (2009). https://doi.org/10.1016/j.engfailanal.2008.02.010
46. Datasheet Additive Manufacturing Powder BÖHLER W360 (2019). Available: https://www.bohler-edelstahl.com/app/uploads/sites/93/2019/02/W360En_AMPO.pdf. Accessed: 3 June 2023

47. K. Fisher, H. Schweiger, J. Hasenberger, H. Dremel, in *Proceedings of the 6th International Tooling Conference: the use of tool steels: experience and research*, ed. by Jens Bergström. New tool steel for warm and hot forging. Karlstad, 10-13 September 2002 (Karlstad Univ., 2002)
48. S. Luo, H. Wang, Z. Gao, Y. Wu, H. Wang, Interaction between high-velocity gas and liquid in gas atomization revealed by a new coupled simulation model. Mater. Des. **212**, 110264 (2021). https://doi.org/10.1016/j.matdes.2021.110264
49. J. Vinčić, A. Aversa, M. Lombardi, D. Manfredi, in *Proceedings of the World PM 2022 Congress*, Repairing D2 tool steel parts by directed energy deposition using a hot work tool steel or a metal matrix composite, World PM2022 Congress & Exhibition, Lyon, 9-13 October 2022 (European Powder Metallurgy Association (EPMA), 2022)
50. F. Deirmina, B. AlMangour, D. Grzesiak, M. Pellizzari, H13–partially stabilized zirconia nanocomposites fabricated by high-energy mechanical milling and selective laser melting. Mater. Des. **146**, 286–297 (2018). https://doi.org/10.1016/j.matdes.2018.03.017
51. T. Ungár, S. Harjo, T. Kawasaki, Y. Tomota, G. Ribárik, Z. Shi, Composite behavior of lath martensite steels induced by plastic strain, a new paradigm for the elastic-plastic response of martensitic steels. Metall. Mater. Trans. A **48**(1), 159–167 (2017). https://doi.org/10.1007/s11661-016-3845-4
52. W.R. Prudente, J.F. Lins, R.P. Siqueira, S.N. Priscila, Microstructural evolution under tempering heat treatment in AISI H13 hot-work tool steel. Int. J. Eng. Res. Appl. **7**(4), 67–71 (2017). https://doi.org/10.9790/9622-0704046771
53. R. Amirarsalani, M. Morakabati, R. Mahdavi, Evaluating hot deformation behavior of W360 tool steel by hot compression test. J. Adv. Mater. Eng. **40**(1), 113–131 (2021). https://doi.org/10.47176/jame.40.1.22122
54. R.A. Grange, C.R. Hribal, L.F. Porter, Hardness of tempered martensite in carbon and low-alloy steels. Metall. Trans. A **8**(11), 1775–1785 (1977). https://doi.org/10.1007/BF02646882
55. Y. Lu, H. Yu, X. Cai, Y. Rong, and R. D. Sisson, Martensite lattice parameter measured by modern X-ray diffraction in Fe-C alloy (2016). Available: https://www.researchgate.net/publication/303364253
56. V. Chaudhary, S.A. Mantri, R.V. Ramanujan, R. Banerjee, Additive manufacturing of magnetic materials. Prog. Mater. Sci. **114**, 100688 (2020). https://doi.org/10.1016/j.pmatsci.2020.100688
57. S. Raju, B.J. Ganesh, A. Banerjee, E. Mohandas, Characterisation of thermal stability and phase transformation energetics in tempered 9Cr–1Mo steel using drop and differential scanning calorimetry. Mater. Sci. Eng. A **465**(1–2), 29–37 (2007). https://doi.org/10.1016/j.msea.2007.01.127
58. R. Casati, M. Coduri, N. Lecis, C. Andrianopoli, M. Vedani, Microstructure and mechanical behavior of hot-work tool steels processed by selective laser melting. Mater. Charact. **137**, 50–57 (2018). https://doi.org/10.1016/j.matchar.2018.01.015